

Metal Nanoparticle Exsolution on a Perovskite Stannate Support with High Electrical Conductivity

Sangbae Yu,¹ Daseob Yoon,¹ Yujeong Lee, Hyojin Yoon, Hyeon Han, Namjo Kim, Cheol-Joo Kim, Kyuwook Ihm, Tae-Sik Oh, and Junwoo Son*

Cite This: *Nano Lett.* 2020, 20, 3538–3544

Read Online

ACCESS |

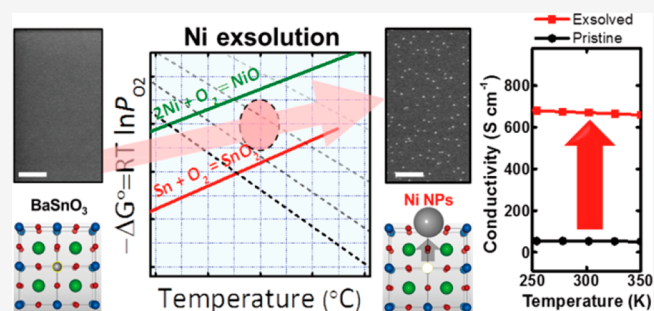
Metrics & More

Article Recommendations

Supporting Information

ABSTRACT: *In situ* exsolution of metal nanoparticles (NPs) is emerging as an alternative technique to deliver thermally stable and evenly dispersed metal NPs, which exhibit excellent adhesion with conducting perovskite oxide supports. Here we provide the first demonstration that Ni metal NPs with high areal density ($\sim 175 \mu\text{m}^{-2}$) and fine size ($\sim 38.65 \text{ nm}$) are exsolved from an A-site-deficient perovskite stannate support ($\text{La}_{0.2}\text{Ba}_{0.7}\text{Sn}_{0.9}\text{Ni}_{0.1}\text{O}_{3-\delta}$ (LBSNO)). The NPs are strongly anchored and impart coking resistance, and the Ni-exsolved stannates show exceptionally high electrical conductivity ($\sim 700 \text{ S}\cdot\text{cm}^{-1}$). The excellent conductivity is attributed to conduction between delocalized Sn 5s orbitals along with structural improvement toward ABO_3 stoichiometry in the stannate support. We also reveal that experimental conditions with strong interaction must be optimized to obtain Ni exsolution without degrading the perovskite stannate framework. Our finding suggests a unique process to induce the formation of metal NPs embedded in stannate with excellent electrical properties.

KEYWORDS: perovskite stannate, exsolution, high electrical conductivity, delocalized orbitals, Ellingham diagram



Significant effort has been devoted to the design of heterogeneous catalysts, i.e., oxide supports that bear catalytically active metal nanoparticles (NPs) on the surface, to simultaneously achieve catalytic activity and high stability.^{1–6} The enhanced performance of the heterogeneous catalysts enables important functions in energy conversion and energy storage, including electrodes for electrocatalysis (i.e., water splitting, solid oxide fuel cells (SOFCs),^{4,7,8} solid oxide electrolyzer cells (SOEC)⁹) and photocatalysis.¹⁰ Along with the catalytically active metal NPs, the oxide support also influences the activity and selectivity of a catalyst by interacting with it at the metal–support interface to affect its electrochemical properties, so the oxide in the heterogeneous catalyst must be selected carefully.^{3–6}

For the integration of metal particles on perovskite oxide (ABO_3) supports, *in situ* exsolution of B-site ions from the ABO_3 lattice in a reducing environment can deliver thermally stable and evenly dispersed metal NPs that adhere strongly to the perovskite oxide support.^{3,7,11–16} For example, *in situ* growth of Ni nanoparticles on a perovskite titanate backbone ($\text{La}_x\text{Sr}_{1-x}\text{TiO}_3$ (LSTO)) was demonstrated to enhance the electrode properties in solid oxide cells.^{7,11–13} However, exsolution has been investigated on perovskite oxides that use *d*-band conduction in transition metal B-site cations;^{11,12,14–16} if a perovskite support can be found that has better electrical and ionic conductivity than these perovskite oxides, electrode performance may be increased further.

Perovskite stannates (e.g., BaSnO_3) exhibit potential as a replacement for existing perovskite oxide supports. BaSnO_3 with the cubic perovskite structure intrinsically is an insulator with a large band gap ($\sim 3.2 \text{ eV}$) but can become a mixed ion–electron conductor at high temperature ($\sim 650 \text{ }^\circ\text{C}$) because La donors in the Ba sites create free electrons,^{17–21} similar to La doping in the Sr sites in SrTiO_3 .²² Unlike SrTiO_3 , whose conduction band for electrons is caused by the localized *3d* orbitals, the conduction band of BaSnO_3 is widely dispersed because it is mainly composed of delocalized Sn 5s orbitals (Figure 1a); La-doped BaSnO_3 (LBSO) has a higher electrical conductivity ($\sim 10^4 \text{ S}\cdot\text{cm}^{-1}$ in single crystals) than any other perovskite oxide conductor and shows excellent room-temperature electron mobility ($\mu_e \approx 320 \text{ cm}^2\cdot\text{V}^{-1}\cdot\text{s}^{-1}$).^{17,19,23} Moreover, BaSnO_3 exhibits excellent ionic conductivity while maintaining chemical and thermal stability and structural integrity even at high temperatures under reducing conditions,^{18,24} so it has been evaluated for energy conversion and storage applications (e.g., batteries,²⁵ fuel cells,²⁶ and photocatalysts^{27–30}). Efficient electrode materials require high

Received: February 5, 2020

Revised: March 18, 2020

Published: April 9, 2020



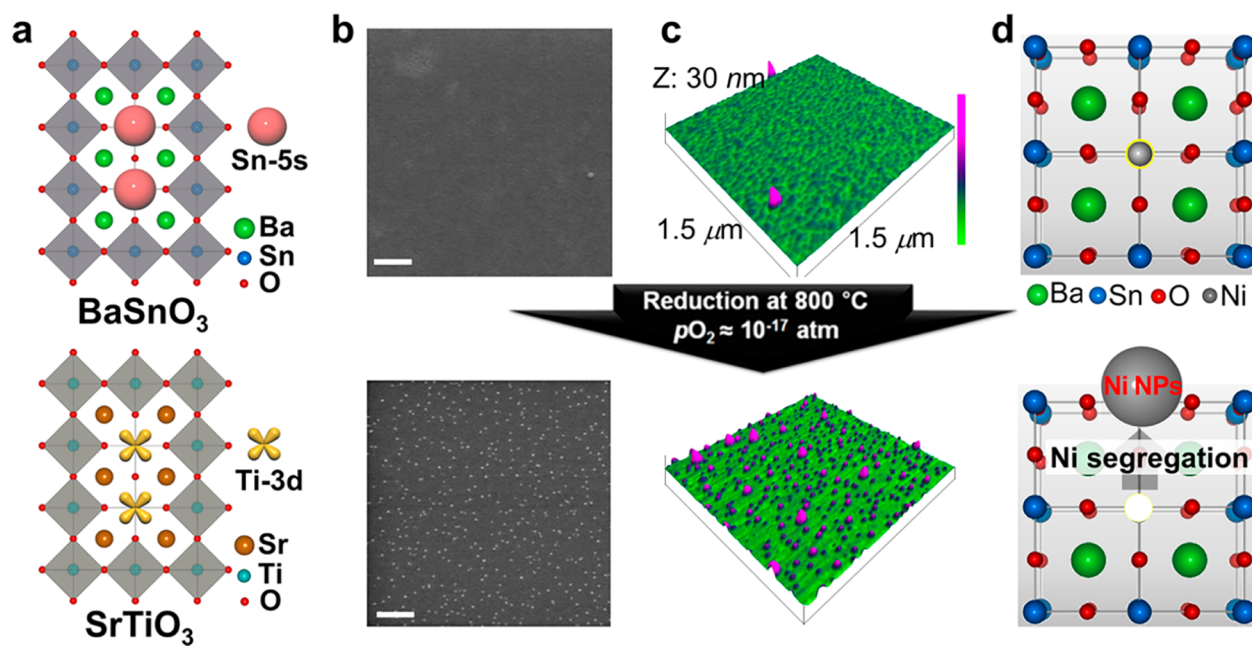


Figure 1. Exsolution of Ni NPs from a perovskite stannate framework (BaSnO₃). (a) Schematic representation of the BaSnO₃ and SrTiO₃ crystal structure and B-site orbitals (Sn 5s and Ti 3d orbitals), which mostly determine electron transport in the conduction bands. (b) SEM micrographs of A-site-deficient Ba_{0.9}Sn_{0.9}Ni_{0.1}O_{3-δ} (BSNO) epitaxial films before and after exsolution. Scale bars = 500 nm. (c) AFM 3D top-view images of the pristine and exsolved BSNO epitaxial films. AFM image area = 1.5 μm × 1.5 μm. (d) Schematic representation of the Ni exsolution process in a reducing atmosphere. Blue circles, Sn ions; green circles, Ba ions; red circles, O ions; gray circles, Ni ions.

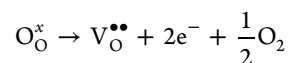
electronic conductivity to transfer electrons smoothly, so stannate-supported electrodes with catalytic NPs would show higher reaction rates and electron/ion transfer than other oxide materials. However, no study has demonstrated a heterogeneous catalyst on a perovskite stannate support, which could significantly increase the electrode performance.

Here we demonstrate exsolution of Ni metal NPs on a perovskite stannate epitaxial support with exceptionally high electrical conductivity and stability for the first time. After a reducing process at high temperature, a large number (~175 particles μm⁻²) of uniformly dispersed Ni particles with an average size of ~38.65 nm were strongly anchored to the surface of the perovskite stannate support. In addition to the structural stability of the exsolved Ni/stannate heterostructures, the stannate support has a high electrical conductivity (~700 S·cm⁻¹), which is more than 10 times higher than that from any titanate support yet reported.^{31,32} As a result of the distinct conduction between delocalized Sn 5s orbitals of the stannate support, the electrical transport was significantly improved by replacing the supporting oxide in the heterostructures.

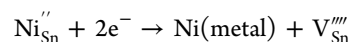
Prior to the exsolution process, perovskite stannate (BaSnO₃) epitaxial films containing 10% Ni dopant were grown on a (001)-oriented SrTiO₃ substrate by pulsed laser deposition (PLD). Since the sizes of Ni²⁺ (0.70 Å) and Sn⁴⁺ (0.69 Å) are similar, Ni dopants are expected to be located at Sn sites in the BaSnO₃ perovskite framework, and the negative charge of the Ni_{Sn}^{''} is compensated by formation of oxygen vacancies (V_O^{••}).³³ A-site-deficient perovskites are more prone to exsolve Ni dopants in the B sites than stoichiometric perovskites, so a 10% Ba-deficient target was intentionally chosen to promote Ni exsolution from Ba_{0.9}Sn_{0.9}Ni_{0.1}O_{3-δ} (BSNO) epitaxial films during the reducing process. Moreover, to increase the electrical conductivity of these perovskite stannate films by La doping in Ba sites, a target containing 20%

La dopant was also ablated to grow La_{0.2}Ba_{0.7}Sn_{0.9}Ni_{0.1}O_{3-δ} (LBSNO) films.^{17,19}

Then the pristine BSNO and LBSNO epitaxial films with atomically flat surfaces were annealed at 800 °C for 5 h under a 0.5% H₂/Ar gas mixture ($p(\text{O}_2) \sim 10^{-17}$ atm). After the annealing process, scanning electron microscopy (SEM) (Figure 1b for BSNO films and Figure S1 for LBSNO films) and atomic force microscopy (AFM) (Figure 1c for BSNO films) showed that the surface was densely (~175 particles μm⁻²) and uniformly populated with exsolved NPs, which increased the root-mean-square roughness (r_{RMS}) from 0.533 to 2.77 nm (Figure 1c for BSNO films). The estimated average size of the exsolved NPs was 38.65 nm (Figures 1b and S2). The areal density and size are comparable to those obtained by Ni exsolution of titanate perovskites (e.g., (La,Sr)_{0.9}(Ti,Ni)₁O_{3-δ} for solid oxide fuel electrodes).^{12,13} The reducing conditions detach oxygen ions from the perovskite stannate lattices to afford electron carriers:^{12,13,20,34,35}



The electrons released by this process nucleate the Ni metal by reduction of the Ni valence state.^{12,13,35} As the reduction proceeds, the Ni nuclei grow by a defect chemical reaction (Figure 1d):^{36,37}



The exsolution phenomenon on the stannate films was locally visualized by cross-sectional scanning transmission electron microscopy (STEM) analysis with elemental mapping of BSNO films after the annealing process (Figures 2a and S3). The exsolved NPs showed only the EDS signal of Ni (Figures 2b,c and S3); this result means that Ni metallic clusters occurred on the surface, as well as in the oxide support; Ni

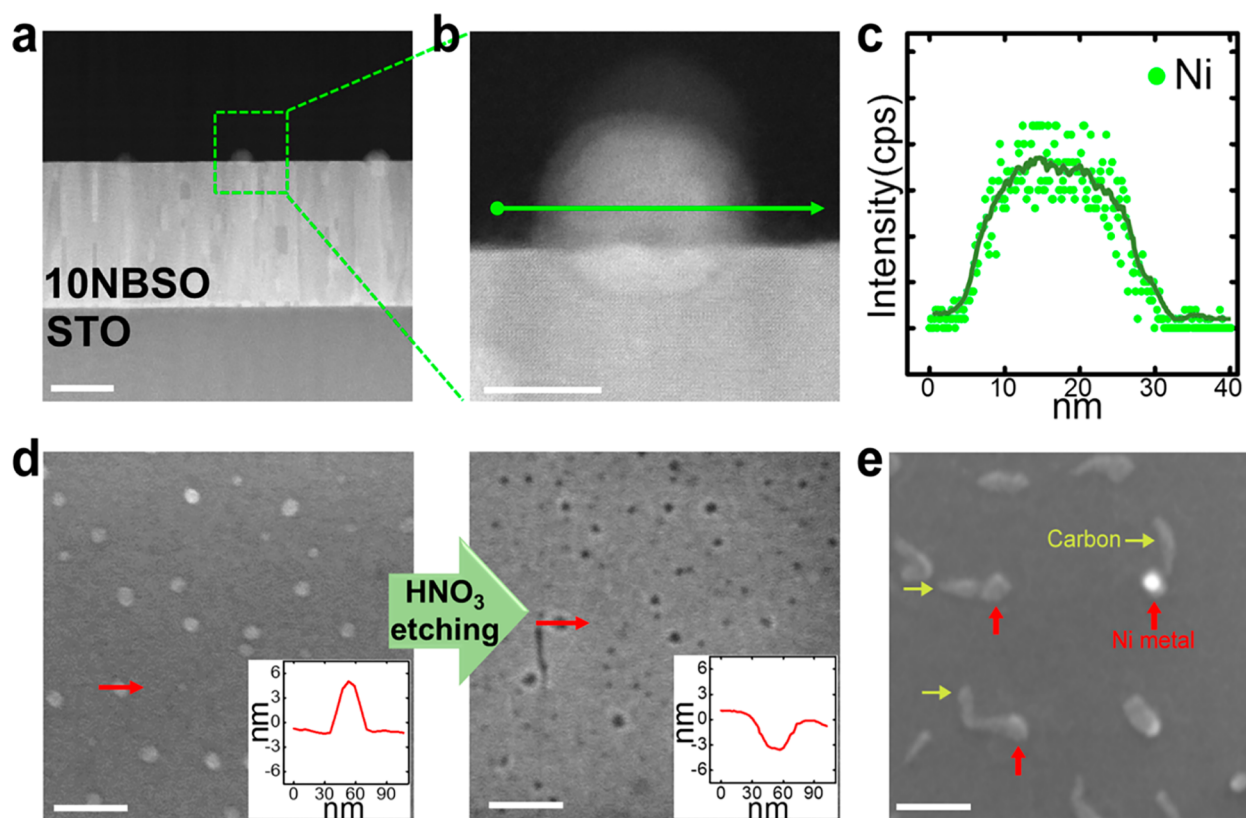


Figure 2. STEM and SEM analysis of an exsolved BSNO film with Ni NPs. (a) Cross-sectional HAADF-STEM image of the exsolved BSNO film. Scale bar = 50 nm. (b) Magnified HAADF-STEM image of the BSNO film near an exsolved NP. Scale bar = 10 nm. (c) Ni element line profile extracted from the arrow in (b) and obtained from STEM-EDS. (d) SEM micrographs of exsolved Ni NPs before and after Ni etching with HNO_3 . The insets show the corresponding line profiles of the Ni particle and etched socket. Scale bars = 200 nm. (e) SEM micrograph after the coking test, showing that carbon fibers (yellow arrows) grow from Ni particles (red arrows) by base growth instead of tip growth. Scale bar = 100 nm.

nuclei from Sn site formed preferentially and selectively in a reducing atmosphere. Interestingly, a STEM image of a socketed Ni NP (~ 4 nm height) shows a $\sim 40\%$ submergence into the stannate surfaces (Figure 2b); this pinned feature implies a strong interaction between the Ni NPs and the stannate support.^{12,13}

The strong interaction of the exsolved Ni NPs with the stannate support was confirmed by the use of SEM to observe the surface topography of the exsolved films after the selective etching of Ni NPs. After Ni NPs with a height of ~ 4 nm (Figure 2d) were selectively etched out using HNO_3 , 3 nm-deep surface pits were formed by removal of the submerged Ni particles with a similar size distribution. Furthermore, we also examined the stability of the exsolved NPs in a hydrocarbon fuel environment (pure CH_4 , 800 °C, 5 h). The interaction between the exsolved Ni NPs and perovskite stannate was strong enough to maintain thermal stability; carbon fibers grow from Ni NPs by base growth instead of by particle lifting induced by tip growth (Figure 2e).^{12,35} This lateral growth of the carbon fibers indicates that the exsolved Ni NPs have a strong coking resistance, which is the main advantage of exsolved particles for use in electrodes at high temperature in fuel cells.^{12,35}

Exsolved LBSNO films also showed excellent electrical conductivity after annealing in a reducing atmosphere (Figure 3a). While both pristine and exsolved BSNO films do not show any conductivity because of the wide band gap of BaSnO_3 (~ 3.6 eV), LBSNO films were metallic (i.e., the conductivity decreased with temperature) because the La dopants in Ba

sites act as carrier-generating degenerate dopants in the BaSnO_3 perovskite framework.^{17,20,21,23} Moreover, after the Ni exsolution process, the room-temperature conductivity (σ_{RT}) was further increased from 54 to ~ 700 $\text{S}\cdot\text{cm}^{-1}$. This conductivity of the stannate support with exsolved Ni particles is at least an order of magnitude higher than that of any titanate support (e.g., ~ 1.8 $\text{S}\cdot\text{cm}^{-1}$ for $\text{SrTi}_{0.75}\text{Nb}_{0.25}\text{O}_3$ ceramic oxide³² and ~ 61 $\text{S}\cdot\text{cm}^{-1}$ for exsolved $\text{La}_{0.2}\text{Sr}_{0.7}\text{Ti}_{0.9}\text{Ni}_{0.1}\text{O}_{3-\delta}$ (LSTNO) films with same thickness (Figure S4)). Although *in situ* conductivity measurement at high temperature is required for application as SOFC electrodes in future studies, the perovskite stannate support can be widely utilized for more general electrocatalysis because of exceptional electron transport at room temperature. The significant improvement in electrical transport in this perovskite oxide with Ni NPs occurs as a result of the fundamental difference in the conduction mechanism, as electron conduction mainly occurs between delocalized Sn 5s orbitals in the stannate support rather than between localized Ti 3d orbitals in the titanate support (Figure 1a).^{18,19}

To further explore the effect of Ni exsolution on the increased conductivity of the stannate support, various X-ray diffraction (XRD) techniques, e.g., symmetrical $2\theta-\omega$ XRD scan (Figure 3b), rocking curves (Figure S5), and reciprocal space mapping (RSM) (Figure 3c), were used to monitor structural changes by crystal defects in the stannate perovskite framework after the exsolution process. Although secondary phases were still absent after the exsolution, the diffraction peak of the (002) BaSnO_3 -related reflection increased, and the

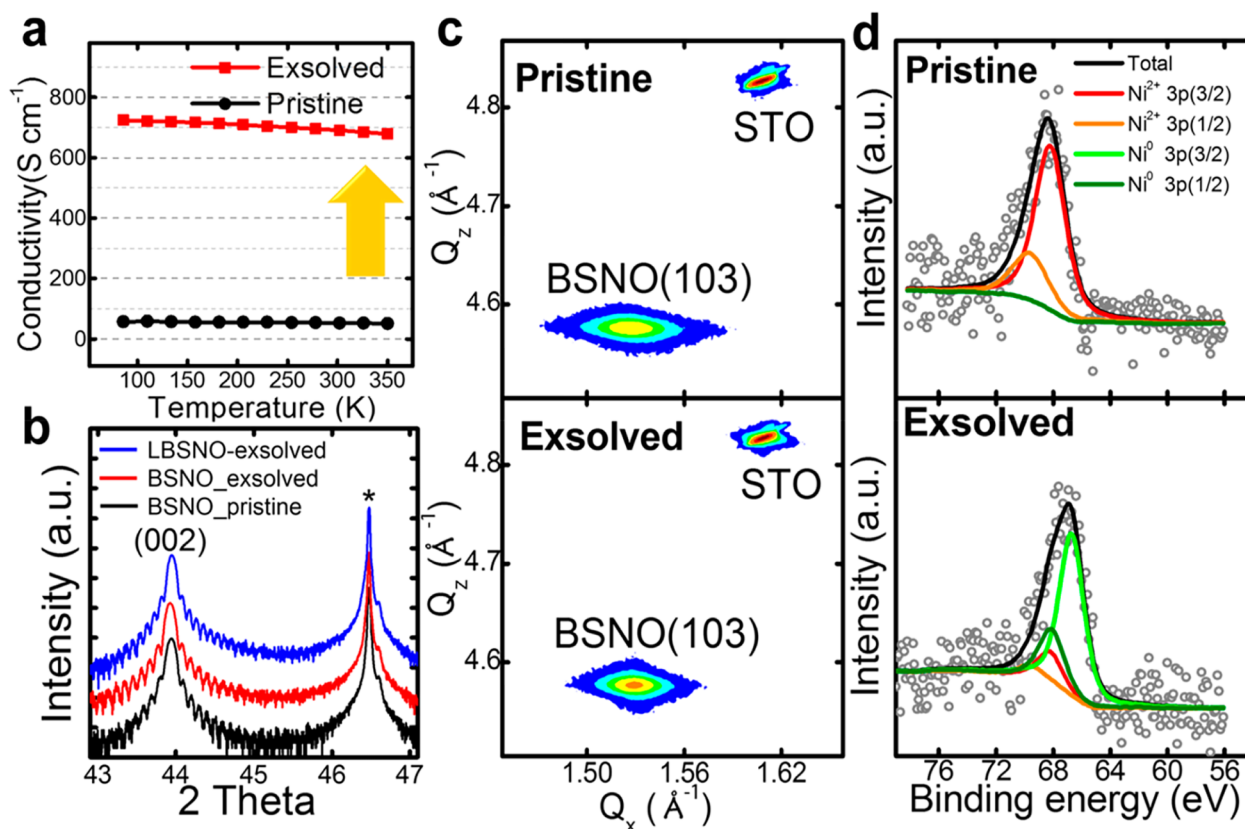


Figure 3. Electrical and structural modulation of (L)BSNO films by Ni exsolution. (a) Temperature-dependent electrical conductivities of pristine (black circles) and exsolved (red squares) LBSNO films. (b) Symmetrical θ - 2θ XRD scan of pristine BSNO and exsolved BSNO and LBSNO films on a SrTiO₃(001) substrate. (c) Reciprocal space mapping (RSM) of (103) reflections from the (top) pristine and (bottom) exsolved BSNO films. (d) Ni 3p spectra of BSNO films (top) before and (bottom) after exsolution obtained using APXPS at a photon energy of 670 eV.

Laue thickness fringe cleared with a slight peak shift to the left in the exsolved BSNO and LBSNO films (Figure 3b). Moreover, the full width at half-maximum (FWHM) of the rocking curve was slightly narrower ($0.058 \rightarrow 0.052 \text{ \AA}^{-1}$) (Figure S5); this result indicates that Ni dopants are highly soluble in Sn sites of pristine BSNO films without the formation of secondary phases,³³ so that the structural quality of the stannate perovskite was maintained (or even improved) in exsolved BSNO films without degradation of the crystal framework after surface segregation of Ni metal from the perovskite lattice.

To elucidate the effect of the exsolution process on the crystallinity of the stannate support, we conducted RSM around the (103) Bragg reflections from pristine and exsolved BSNO films (Figure 3c). At first glance, the (103) reflection of the exsolved BSNO films had a higher peak intensity and narrower peak width than those of pristine films, consistent with the results from the symmetrical scan and rocking curves. Quantitative investigation of RSM revealed that the lattice volume was slightly increased from 69.697 to 69.833 \AA^3 after the reducing process, which indicates that some oxygen atoms in the BSNO films are released from the stannate lattice by forming additional oxygen vacancies after exsolution.²⁰ At the same time, the FWHM of the in-plane direction was decreased from 0.0705 to 0.0482 \AA^{-1} ; a significant decrease in the number of extended defects (e.g., of crystal mosaicity related to dislocations and of low-angle grain boundaries) occurs at the expense of anion vacancy generation in the stannate support.²⁰

With regard to control of the cation stoichiometry, A-site (Ba-site) deficiency was initially used to design systems that exsolve the B sites in the perovskite stannate, so exsolution of Ni from the B site acts to locally revert the perovskite to a “defect-free” ABO₃ stoichiometry.¹¹ Therefore, high-temperature exsolution leads to a decrease in the number of extended defects in the (L)BSNO support as well as spontaneous adjustment of the cation stoichiometry; these changes contribute to the increase in conductivity after exsolution.

To directly monitor the nucleation and growth of Ni metal at the stannate surface in real time, *in situ* ambient-pressure X-ray photoemission spectroscopy (APXPS) was performed during the exsolution process of BSNO epitaxial films. First, to remove possible surface contaminants before the exsolution, the samples were carefully cleaned by heating at $250 \text{ }^\circ\text{C}$ in 100 mTorr O_2 ; the contaminant-related C 1s peak completely disappeared after surface cleaning (Figure S6). Then, to characterize the dynamic modulation of surface states in contaminant-free BSNO epitaxial films under a H₂ pressure of 20 mTorr during the exsolution, the Ni 3p and Sn 3d spectra were acquired using APXPS at a photon energy of 670 eV with inelastic mean free paths in the range of $\sim 1.0 \text{ nm}$.³⁸ Before exsolution, the Ni 3p had binding energy (E_b) of $\sim 68.4 \text{ eV}$ and Sn 3d had an E_b of $\sim 486.8 \text{ eV}$. After H₂ gas had been introduced at $400 \text{ }^\circ\text{C}$, both E_b values gradually decreased (~ 68.4 to $\sim 66.9 \text{ eV}$ for Ni 3p and ~ 486.8 to $\sim 486.6 \text{ eV}$ for Sn 3d) as exsolution proceeded (Figures 3d and S7).

For quantitative analysis, each spectrum was deconvoluted using Lorentzian–Gaussian curves after background subtrac-

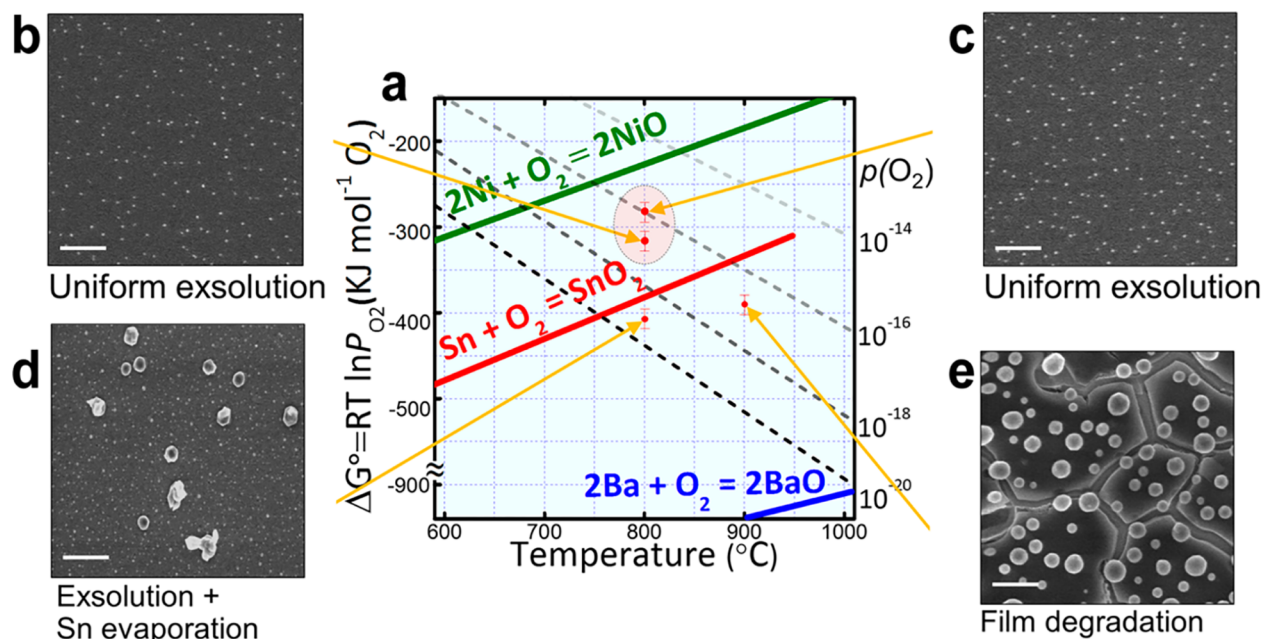


Figure 4. Effect of annealing temperature and oxygen partial pressure on Ni NP exsolution on the stannate support. (a) Annealing condition for the BSNO film (red circles) together with $p(\text{O}_2)$ plots of binary oxides and metals. The green, red, and blue lines mark Ni, Sn, and Ba Ellingham curves of binary oxides, respectively. (b–e) Plane-view SEM images that correspond to each point with different thermodynamic variables (scale bars = 1 μm). Ni exsolution occurred under conditions within the red ellipse.

tion (Figure 3d). Before the exsolution process, most Ni $3p$ spectra could be assigned to the $\text{Ni}^{2+} 3p_{3/2}$ peak ($E_b \approx 68.3$ eV) or the $\text{Ni}^{2+} 3p_{1/2}$ peak ($E_b \approx 69.8$ eV);³⁵ this result means that the Ni ions were in the perovskite lattice. As the exsolution proceeded, the intensities of the deconvoluted $\text{Ni}^0 3p_{3/2}$ ($E_b \approx 66.7$ eV) and $\text{Ni}^0 3p_{1/2}$ ($E_b \approx 68.2$ eV) peaks³⁵ gradually increased at the expense of the $\text{Ni}^{2+} 3p_{3/2}$ and $\text{Ni}^{2+} 3p_{1/2}$ peaks, which directly shows the emergence of metallic Ni NPs on the surface from the reduction of Ni^{2+} in the stannate lattice. The fraction of the metallic $\text{Ni}^0 3p$ peak increased from 0.01% to 88.77% as the exsolution time increased (Figures S7 and S8). This observation confirms that catalytically active Ni ions, which are substituted in the host stannate lattice to form a solid solution, are released (exsolved) onto the surface as Ni metal particles once the oxide lattice has been sufficiently reduced.

A question that remains to be addressed is how the thermodynamic parameters (i.e., the annealing temperature T and oxygen partial pressure $p(\text{O}_2)$) affect the evolution of Ni NPs on the stannate support during the exsolution process. The exsolution process is thermodynamically driven by a reduction of the total free energy of the system, then reorganized by kinetic migration toward the surface; the prerequisite for the exsolution process is thermodynamic stability of the formation of Ni NPs on the perovskite oxide, as long as sufficient kinetics is allowed.

For thermodynamic analysis, the annealing conditions for exsolved BSNO films are marked by the red circles in Figure 4a on the magnified part of the Ellingham curves of binary oxides ($2\text{Ni} + \text{O}_2 \rightleftharpoons 2\text{NiO}$, $\text{Sn} + \text{O}_2 \rightleftharpoons \text{SnO}_2$, $2\text{Ba} + \text{O}_2 \rightleftharpoons 2\text{BaO}$) as functions of T and $p(\text{O}_2)$, which can be determined by the dotted lines.^{39,40} Since the Ellingham curves indicate the equilibrium between metal and binary oxides, $p(\text{O}_2)$ regions higher than the Ellingham curves of metals represent thermodynamic stability of the metal oxides.^{39,40} In principle, to form metallic Ni without degrading the perovskite oxide

framework, the thermodynamic variables (T and $p(\text{O}_2)$) should be favorable for the formation of metallic Ni (i.e., below the Ni Ellingham curve) and unfavorable for the decomposition of other chemical elements in BSNO films (i.e., above the Sn (or Ba) Ellingham diagram). Thus, the optimal thermodynamic condition for metallic Ni exsolution in the BSNO perovskite framework (Figure 4a, red ellipse) is $\Delta G^\circ(\text{Sn} + \text{O}_2 \rightleftharpoons \text{SnO}_2) < \Delta G^\circ(T, p(\text{O}_2)) < \Delta G^\circ(2\text{Ni} + \text{O}_2 \rightleftharpoons 2\text{NiO})$. Indeed, uniform exsolution of Ni NPs was achieved without degradation of the BSNO support in this theoretically predicted thermodynamic region ($p(\text{O}_2) \sim 10^{-17}$ or 10^{-16} atm at 800 °C for 5 h) as observed with SEM (Figure 4b,c). Thus, the above thermodynamic conditions determine the experimental window that allows uniform Ni exsolution on a stable stannate support. We also carried out the exsolution process within the “exsolution” window ($p_{\text{O}_2} \sim 10^{-17}$ atm at 800 °C) in the Ellingham diagram using $\text{Ba}_{0.9}\text{Sn}_{0.9}\text{Ni}_{0.1}\text{O}_{3-\delta}$ (BSNO) ceramic powder. Ni nanoparticles with similar diameter are exsolved on the surface of BSNO ceramic powder after the reducing annealing (Figure S9); the thermodynamic condition for Ni exsolution on perovskite stannate is generally applicable to any sample geometry.

When $p(\text{O}_2)$ was further lowered below the Ellingham curve for Sn (i.e., $p(\text{O}_2) \sim 10^{-19}$ atm at 800 °C for 5 h), microsized BaO precipitates formed on the BSNO film surface along with exsolution of Ni NPs (Figure 4d). The thermodynamic conditions are below the Ellingham curve for Sn, so the BaSnO_3 perovskite framework is likely to decompose under excessive reducing conditions, and as a result, highly volatile Sn metal or SnO may evaporate; this process leads to the formation of residual BaO precipitates.^{41–43} Then, when the reduction temperature was increased ($T = 900$ °C) with $p(\text{O}_2) \sim 10^{-17}$ atm, the stannate support was significantly degraded by formation of microsized cracks and BaO precipitates (Figure 4e); these thermodynamic and kinetic conditions accelerate the loss of Sn-related phases under this high-

temperature reducing process, which gives rise to an unstable crystal framework of the stannate support with the perovskite structure.

In summary, *in situ* growth of uniformly dispersed Ni NPs on a perovskite stannate ((L)BSNO) backbone was first achieved by controlling the thermodynamic driving force that rearranges the atoms at and near the surface. By precise control of the thermodynamic variables ($p(\text{O}_2) \sim 10^{-17}$ or 10^{-16} atm at 800 °C for 5 h) for the uniform exsolution of Ni NPs without the degradation of BSNO support, Ni metal cations dissolved in a Sn site exsolved from the stannate lattice under reducing conditions and then spontaneously condensed into fine and uniformly dispersed Ni metal NPs with strong interaction and stability embedded in the oxide surface. In particular, excellent electrical conductivity ($\sim 700 \text{ S}\cdot\text{cm}^{-1}$) was achieved as a result of electron conduction between delocalized *s* orbitals in the stannate support with Ni NPs. Our *in situ* exsolution process by thermodynamic driving force offers an opportunity to design new heterostructures that bear metal NPs and perovskite oxide to obtain excellent electrical transport and also to efficiently manufacture uniform and numerous metal NPs on highly conductive perovskite stannates.

■ ASSOCIATED CONTENT

Supporting Information

The Supporting Information is available free of charge at <https://pubs.acs.org/doi/10.1021/acs.nanolett.0c00488>.

SEM of LBSNO films before and after exsolution; distribution of Ni particle size; STEM analysis with elemental mapping of exsolved BSNO films; potentials of LBSNO films as promising SOFC electrodes; quantitative comparison between the pristine and exsolved BSNO films using SEM, AFM, and XRD; XPS survey spectra; quantification of the XPS Ni 3*p* and Sn 3*d* spectra; Ni *L*₃-edge XAS spectra; SEM of the pristine and exsolved BSNO ceramic powder; SEM of exsolved BSNO films with different thicknesses; experimental methods (PDF)

■ AUTHOR INFORMATION

Corresponding Author

Junwoo Son – Department of Materials Science and Engineering, Pohang University of Science and Technology (POSTECH), Pohang 37673, Republic of Korea; orcid.org/0000-0002-5363-1987; Email: jwson@postech.ac.kr

Authors

Sangbae Yu – Department of Materials Science and Engineering, Pohang University of Science and Technology (POSTECH), Pohang 37673, Republic of Korea

Daseob Yoon – Department of Materials Science and Engineering, Pohang University of Science and Technology (POSTECH), Pohang 37673, Republic of Korea

Yujeong Lee – Department of Materials Science and Engineering, Pohang University of Science and Technology (POSTECH), Pohang 37673, Republic of Korea

Hyojin Yoon – Department of Materials Science and Engineering, Pohang University of Science and Technology (POSTECH), Pohang 37673, Republic of Korea

Hyeon Han – Department of Materials Science and Engineering, Pohang University of Science and Technology (POSTECH),

Pohang 37673, Republic of Korea; orcid.org/0000-0002-2973-5225

Namjo Kim – Department of Chemical Engineering, Pohang University of Science and Technology (POSTECH), Pohang 37673, Republic of Korea

Cheol-Joo Kim – Department of Chemical Engineering, Pohang University of Science and Technology (POSTECH), Pohang 37673, Republic of Korea; orcid.org/0000-0002-4312-3866

Kyuwook Ihm – Pohang Accelerator Laboratory, Pohang 37673, Republic of Korea

Tae-Sik Oh – Department of Chemical Engineering, Auburn University, Auburn, Alabama 36849, United States

Complete contact information is available at: <https://pubs.acs.org/doi/10.1021/acs.nanolett.0c00488>

Author Contributions

[†]S.Y. and D.Y. contributed equally to this work. J.S., S.Y., and D.Y. conceived the idea and designed the study; S.Y. and D.Y. performed the film growth, X-ray diffraction, and transport measurements with the assistance of Y.L. and H.H.; S.Y., H.Y., K.I., and J.S. performed the synchrotron X-ray spectroscopy; S.Y. performed the carbon coking experiment with the assistance of N.K. and C.-J.K.; J.S., S.Y., and D.Y. wrote the manuscript, and all of the authors commented on it; J.S. directed the overall research.

Notes

The authors declare the following competing financial interest(s): S.Y., D.Y. and J.S. are co-inventors on a patent application based on the results of this work filed by Pohang University of Science and Technology.

■ ACKNOWLEDGMENTS

We acknowledge support for this work from the Basic Science Research Program (2020R1A2C2006389) through the National Research Foundation of Korea (NRF) funded by the Ministry of Science and ICT. N.K. and C.-J.K. were supported by the Basic Science Research Program (2017R1D1A1B03034896) through the NRF funded by the Ministry of Science and ICT. This research used resources of the Advanced Light Source, a DOE Office of Science User Facility, under Contract DE-AC02-05CH11231. We thank K. J. Kim for the discussion and assistance with the synthesis of the (L)BSNO target and K.-J. Lee and E. J. Crumlin for the assistance with the APXPS.

■ REFERENCES

- (1) Farmer, J. A.; Campbell, C. T. Ceria Maintains Smaller Metal Catalyst Particles by Strong Metal-Support Bonding. *Science* **2010**, *329*, 933–936.
- (2) White, R. J.; Luque, R.; Budarin, V. L.; Clark, J. H.; Macquarrie, D. J. Supported metal nanoparticles on porous materials. Methods and applications. *Chem. Soc. Rev.* **2009**, *38*, 481–494.
- (3) Irvine, J. T. S.; Neagu, D.; Verbraeken, M. C.; Chatzichristodoulou, C.; Graves, C.; Mogensen, M. B. Evolution of the electrochemical interface in high-temperature fuel cells and electrolyzers. *Nat. Energy* **2016**, *1*, 15014.
- (4) Cowin, P. I.; Petit, C. T.; Lan, R.; Irvine, J. T.; Tao, S. Recent progress in the development of anode materials for solid oxide fuel cells. *Adv. Energy Mater.* **2011**, *1*, 314–332.
- (5) Jung, W.; Gu, K. L.; Choi, Y.; Haile, S. M. Robust nanostructures with exceptionally high electrochemical reaction activity for high temperature fuel cell electrodes. *Energy Environ. Sci.* **2014**, *7*, 1685–1692.

- (6) Choi, Y.; Cha, S. K.; Ha, H.; Lee, S.; Seo, H. K.; Lee, J. Y.; Kim, H. Y.; Kim, S. O.; Jung, W. Unravelling inherent electrocatalysis of mixed-conducting oxide activated by metal nanoparticle for fuel cell electrodes. *Nat. Nanotechnol.* **2019**, *14*, 245–251.
- (7) Myung, J.-h.; Neagu, D.; Miller, D. N.; Irvine, J. T. Switching on electrocatalytic activity in solid oxide cells. *Nature* **2016**, *537*, 528.
- (8) Zhu, T.; Troiani, H. E.; Mogni, L. V.; Han, M.; Barnett, S. A. Ni-substituted Sr(Ti, Fe)O₃ SOFC anodes: achieving high performance via metal alloy nanoparticle exsolution. *Joule* **2018**, *2*, 478–496.
- (9) Tsekouras, G.; Neagu, D.; Irvine, J. T. Step-change in high temperature steam electrolysis performance of perovskite oxide cathodes with exsolution of B-site dopants. *Energy Environ. Sci.* **2013**, *6*, 256–266.
- (10) Ebina, Y.; Sasaki, T.; Harada, M.; Watanabe, M. Restacked perovskite nanosheets and their Pt-loaded materials as photocatalysts. *Chem. Mater.* **2002**, *14*, 4390–4395.
- (11) Neagu, D.; Tsekouras, G.; Miller, D. N.; Ménard, H.; Irvine, J. T. In situ growth of nanoparticles through control of non-stoichiometry. *Nat. Chem.* **2013**, *5*, 916.
- (12) Neagu, D.; Oh, T.-S.; Miller, D. N.; Ménard, H.; Bukhari, S. M.; Gamble, S. R.; Gorte, R. J.; Vohs, J. M.; Irvine, J. T. Nano-socketed nickel particles with enhanced coking resistance grown in situ by redox exsolution. *Nat. Commun.* **2015**, *6*, 8120.
- (13) Kim, K. J.; Han, H.; Defferriere, T.; Yoon, D.; Na, S.; Kim, S. J.; Dayaghi, A. M.; Son, J.; Oh, T. S.; Jang, H. M.; Choi, G. M. Facet-Dependent in Situ Growth of Nanoparticles in Epitaxial Thin Films: The Role of Interfacial Energy. *J. Am. Chem. Soc.* **2019**, *141*, 7509–7517.
- (14) Nishihata, Y.; Mizuki, J.; Akao, T.; Tanaka, H.; Uenishi, M.; Kimura, M.; Okamoto, T.; Hamada, N. Self-regeneration of a Pd-perovskite catalyst for automotive emissions control. *Nature* **2002**, *418*, 164–167.
- (15) Kwak, N. W.; Jeong, S. J.; Seo, H. G.; Lee, S.; Kim, Y.; Kim, J. K.; Byeon, P.; Chung, S. Y.; Jung, W. In situ synthesis of supported metal nanocatalysts through heterogeneous doping. *Nat. Commun.* **2018**, *9*, 4829.
- (16) Jo, Y. R.; Koo, B.; Seo, M. J.; Kim, J. K.; Lee, S.; Kim, K.; Han, J. W.; Jung, W.; Kim, B. J. Growth Kinetics of Individual Co Particles Ex-solved on SrTi_{0.75}Co_{0.25}O_{3-δ} Polycrystalline Perovskite Thin Films. *J. Am. Chem. Soc.* **2019**, *141*, 6690–6697.
- (17) Kim, H. J.; Kim, U.; Kim, H. M.; Kim, T. H.; Mun, H. S.; Jeon, B.-G.; Hong, K. T.; Lee, W.-J.; Ju, C.; Kim, K. H.; Char, K. High Mobility in a Stable Transparent Perovskite Oxide. *Appl. Phys. Express* **2012**, *5*, 061102.
- (18) Ismail-Beigi, S.; Walker, F. J.; Cheong, S.-W.; Rabe, K. M.; Ahn, C. H. Alkaline earth stannates: The next silicon? *APL Mater.* **2015**, *3*, 062510.
- (19) Lee, W. J.; Kim, H. J.; Kang, J.; Jang, D. H.; Kim, T. H.; Lee, J. H.; Kim, K. H. Transparent Perovskite Barium Stannate with High Electron Mobility and Thermal Stability. *Annu. Rev. Mater. Res.* **2017**, *47*, 391–423.
- (20) Yoon, D.; Yu, S.; Son, J. Oxygen vacancy-assisted recovery process for increasing electron mobility in n-type BaSnO₃ epitaxial thin films. *NPG Asia Mater.* **2018**, *10*, 363–371.
- (21) Yu, S.; Yoon, D.; Son, J. Enhancing electron mobility in La-doped BaSnO₃ thin films by thermal strain to annihilate extended defects. *Appl. Phys. Lett.* **2016**, *108*, 262101.
- (22) Son, J.; Moetakef, P.; Jalan, B.; Bierwagen, O.; Wright, N. J.; Engel-Herbert, R.; Stemmer, S. Epitaxial SrTiO₃ films with electron mobilities exceeding 30,000 cm² V⁻¹ s⁻¹. *Nat. Mater.* **2010**, *9*, 482–484.
- (23) Prakash, A.; Xu, P.; Faghaninia, A.; Shukla, S.; Ager, J. W., III; Lo, C. S.; Jalan, B. Wide bandgap BaSnO₃ films with room temperature conductivity exceeding 10⁴ S cm⁻¹. *Nat. Commun.* **2017**, *8*, 15167.
- (24) Lee, W. J.; Kim, H. J.; Sohn, E.; Kim, H. M.; Kim, T. H.; Char, K.; Kim, J. H.; Kim, K. H. Oxygen diffusion process in a Ba_{0.96}La_{0.04}SnO₃ thin film on SrTiO₃(001) substrate as investigated by time-dependent Hall effect measurements. *Phys. Status Solidi A* **2015**, *212*, 1487–1493.
- (25) Nithyadharseni, P.; Reddy, M.; Ozoemena, K. I.; Ezema, F. I.; Balakrishna, R. G.; Chowdari, B. Electrochemical performance of BaSnO₃ anode material for lithium-ion battery prepared by molten salt method. *J. Electrochem. Soc.* **2016**, *163*, A540–A545.
- (26) Hussain, A. M.; Pan, K.-J.; Robinson, I. A.; Hays, T.; Wachsmann, E. D. Stannate-based ceramic oxide as anode materials for oxide-ion conducting low-temperature solid oxide fuel cells. *J. Electrochem. Soc.* **2016**, *163*, F1198–F1205.
- (27) Borse, P. H.; Joshi, U. A.; Ji, S. M.; Jang, J. S.; Lee, J. S.; Jeong, E. D.; Kim, H. G. Band gap tuning of lead-substituted BaSnO₃ for visible light photocatalysis. *Appl. Phys. Lett.* **2007**, *90*, 034103.
- (28) Yuan, Y.; Lv, J.; Jiang, X.; Li, Z.; Yu, T.; Zou, Z.; Ye, J. Large impact of strontium substitution on photocatalytic water splitting activity of BaSnO₃. *Appl. Phys. Lett.* **2007**, *91*, 094107.
- (29) Sales, H. B.; Bouquet, V.; Députier, S.; Ollivier, S.; Gouttefangeas, F.; Guilloux-Viry, M.; Dorcet, V.; Weber, I. T.; de Souza, A. G.; Dos Santos, I. M. G. Sr_{1-x}Ba_xSnO₃ system applied in the photocatalytic discoloration of an azo-dye. *Solid State Sci.* **2014**, *28*, 67–73.
- (30) Kim, M.; Lee, B.; Ju, H.; Kim, J. Y.; Kim, J.; Lee, S. W. Oxygen-Vacancy-Introduced BaSnO_{3-δ} Photoanodes with Tunable Band Structures for Efficient Solar-Driven Water Splitting. *Adv. Mater.* **2019**, *31*, 1903316.
- (31) Li, X.; Zhao, H.; Xu, N.; Zhou, X.; Zhang, C.; Chen, N. Electrical conduction behavior of La, Co co-doped SrTiO₃ perovskite as anode material for solid oxide fuel cells. *Int. J. Hydrogen Energy* **2009**, *34*, 6407–6414.
- (32) Arrivé, C.; Delahaye, T.; Joubert, O.; Gauthier, G. Exsolution of nickel nanoparticles at the surface of a conducting titanate as potential hydrogen electrode material for solid oxide electrochemical cells. *J. Power Sources* **2013**, *223*, 341–348.
- (33) Upadhyay, S.; Parkash, O.; Kumar, D. Solubility of lanthanum, nickel and chromium in barium stannate. *Mater. Lett.* **2001**, *49*, 251–255.
- (34) Scanlon, D. O. Defect engineering of BaSnO₃ for high-performance transparent conducting oxide applications. *Phys. Rev. B: Condens. Matter Mater. Phys.* **2013**, *87*, 161201.
- (35) Han, H.; Park, J.; Nam, S. Y.; Kim, K. J.; Choi, G. M.; Parkin, S. S. P.; Jang, H. M.; Irvine, J. T. S. Lattice strain-enhanced exsolution of nanoparticles in thin films. *Nat. Commun.* **2019**, *10*, 1471.
- (36) Sun, Y.-F.; Zhang, Y.-Q.; Chen, J.; Li, J.-H.; Zhu, Y.-T.; Zeng, Y.-M.; Amirkhiz, B. S.; Li, J.; Hua, B.; Luo, J.-L. New opportunity for in situ exsolution of metallic nanoparticles on perovskite parent. *Nano Lett.* **2016**, *16*, 5303–5309.
- (37) Gao, Y.; Lu, Z.; You, T. L.; Wang, J.; Xie, L.; He, J.; Ciucci, F. Energetics of Nanoparticle Exsolution from Perovskite Oxides. *J. Phys. Chem. Lett.* **2018**, *9*, 3772–3778.
- (38) Seah, M. P.; Dench, W. Quantitative electron spectroscopy of surfaces: A standard data base for electron inelastic mean free paths in solids. *Surf. Interface Anal.* **1979**, *1*, 2–11.
- (39) Ellingham, H. J. T. Reducibility of oxides and sulphides in metallurgical processes. *J. Soc. Chem. Ind., London* **1944**, *63*, 125–133.
- (40) Robino, C. V. Representation of mixed reactive gases on free energy (Ellingham–Richardson) diagrams. *Metall. Mater. Trans. B* **1996**, *27*, 65–69.
- (41) Galazka, Z.; Uecker, R.; Irmscher, K.; Klimm, D.; Bertram, R.; Kwasniewski, A.; Naumann, M.; Schewski, R.; Pietsch, M.; Juda, U.; Fiedler, A.; Albrecht, M.; Ganschow, S.; Markurt, T.; Gugushev, C.; Bickermann, M. Melt growth and properties of bulk BaSnO₃ single crystals. *J. Phys.: Condens. Matter* **2017**, *29*, 075701.
- (42) Lee, W. J.; Lee, H.; Ko, K. T.; Kang, J.; Kim, H. J.; Lee, T.; Park, J. H.; Kim, K. H. Realization of an atomically flat BaSnO₃(001) substrate with SnO₂ termination. *Appl. Phys. Lett.* **2017**, *111*, 231604.
- (43) Rodenbucher, C.; Meuffels, P.; Speier, W.; Ermrich, M.; Wrana, D.; Krok, F.; Szot, K. Stability and Decomposition of Perovskite-Type Titanates upon High-Temperature Reduction. *Phys. Status Solidi RRL* **2017**, *11*, 1700222.